ACS APPLIED MATERIALS & INTERFACES
Research Article
www.acsami.org

Synthesis and Characterization of Nanostructured Stannite $Cu_2ZnSnSe_4$ and $Ag_2ZnSnSe_4$ for Thermoelectric Applications

Kaya Wei and George S. Nolas*

Department of Physics, University of South Florida, Tampa, Florida 33620, United States

ABSTRACT: $Cu_2ZnSnSe_4$ and $Ag_2ZnSnSe_4$ nanocrystals were synthesized by a colloidal synthesis route and subsequently densified to form dense polycrystalline bulk specimens with nanoscale grains employing spark plasma sintering (SPS). Powder X-ray diffraction (XRD), transmission electron microscopy (TEM), and electron diffraction spectroscopy (EDS) were used to characterize the nanocrystals. The optical bandgap, thermal stability, and low temperature transport properties of the nanostructured polycrystalline stannites $Cu_2ZnSnSe_4$ and $Ag_2ZnSnSe_4$ were investigated. The transport properties of $Ag_2ZnSnSe_4$ are reported here for the first time and indicate polaronic-type conduction. $Cu_2ZnSnSe_4$ is p-type while $Ag_2ZnSnSe_4$ is n-type. The thermal transport in these materials is also investigated, the thermal conductivity of nanostructured $Cu_2ZnSnSe_4$ being greatly reduced compared with that of the bulk. Our results are presented in light of the interest in these materials for thermoelectric applications.

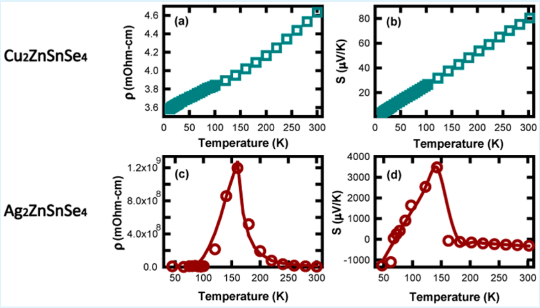

KEYWORDS: *quaternary stannites, colloidal synthesis, SPS, nanostructured bulk, transport properties*

■ INTRODUCTION

Quaternary chalcogenides form a large class of materials composed of earth-abundant and nontoxic elements that have been studied over the past decade for a variety of different applications, including solar-cell absorbers,[1,2] photocatalysts for solar water splitting,[3] nonlinear optics,[4] topological insulators,[5] and magneto-optic and magneto-ferroics.[6,7] Very recently, certain compositions have also shown promising thermoelectric properties due to their relatively low thermal conductivity, κ, in addition to the fact that good electrical properties can be achieved by appropriate doping.[8−11] For several chalcogenide materials, nanoscale effects can directly affect the transport properties and result in enhanced thermoelectric performance;[12−14] however, both p- and n-type compositions are required in thermoelectric devices.[15] Herein, we investigate the low temperature transport properties of the n-type stannite compound $Ag_2ZnSnSe_4$ in comparison to that of p-type $Cu_2ZnSnSe_4$.

Interfacial phonon and charge carrier scattering in dense bulk materials that contain nanoscale grains or domains have been shown to possess enhanced thermoelectric properties as compared to that of bulk materials.[16−18] Thus, certain thermoelectric materials that contain nanoscale domains offer improved thermoelectric properties over that of the bulk,[18−27] as has also been shown to be the case for $Cu_2CdSnSe_4$,[9] Cu_2ZnSnS_4,[28] and $Cu_2ZnGeSe_4$.[29] Employing a bottom-up approach, nanostructured polycrystalline $Cu_2ZnSnSe_4$ and $Ag_2ZnSnSe_4$ were synthesized by solution-phase processing followed by densification by spark plasma sintering (SPS). The colloidal method reported here can be applied for the synthesis of other Ag-based quaternary stannites. Our goal is to investigate and compare the low temperature transport properties of nanostructured $Cu_2ZnSnSe_4$ and $Ag_2ZnSnSe_4$ in light of the recent interest in quaternary chalcogenides for thermoelectric applications.[9,11,28,29]

■ EXPERIMENTAL SECTION

The chemicals used in this study were copper(II) acetate monohydrate [$Cu(OOCCH_3)\cdot H_2O$] (98%, Alfa Aesar), silver acetate [$C_2H_3AgO_2$] (99.99%, Sigma-Aldrich), zinc acetate dihydrate [$Zn(CH_3COO)_2\cdot 2H_2O$] (97%, Alfa Aesar), tin(II) chloride dihydrate [$SnCl_2\cdot 2H_2O$] (98%, Alfa Aesar), selenium powder (99.999%, Alfa Aesar), and Oleylamine (80%, Acros Organics). All chemicals were used as received without further purification. In a typical synthesis, 1 mmol of $Cu(OOCCH_3)\cdot H_2O$ or $C_2H_3AgO_2$, 0.5 mmol of $Zn(CH_3COO)_2\cdot 2H_2O$, 0.5 mmol of $SnCl_2\cdot 2H_2O$, 2 mmol of Se powder, and 15 mL of Oleylamine were loaded into a three-neck flask on a Schlenk line. The mixture was kept at room temperature under a N_2 flow for 10 min followed by degassing under vacuum for 100 min. A dark brown color was observed for both syntheses during degassing. The solution was then heated to 110 °C for 30 min followed by heating to a reaction temperature of 280 °C for another 30 min under N_2 flow for nanoparticle growth. The flask was then rapidly cooled to room temperature in an ice water bath. A typical ethanol/chloroform mixture was used to wash the products three times in total; then, they were isolated by centrifugation at 9000 rpm for 3 min. The final products were transferred to a vacuum oven for drying before structural and chemical analyses.

The as-synthesized products were characterized by powder X-ray diffraction (XRD, Bruker AXS D8), PowderCell (PCW), transmission electron microscopy (TEM, JEOL 2010F transmission electron

Received: February 19, 2015
Accepted: April 20, 2015
Published: April 20, 2015

ACS Publications

DOI: 10.1021/acsami.5b01617
ACS Appl. Mater. Interfaces 2015, 7, 9752−9757

microscope operated at 200 kV with Cs = 1.0 mm), and electron diffraction spectroscopy (EDS). TEM images and electron diffraction patterns were acquired with a Gatan Orius SC200B digital camera while EDS data was collected using an Oxford Instruments INCA EDS system. Differential thermal analysis (DTA, TA Instruments, Q600) was used to investigate the thermal stability and dissociation temperature of the nanocrystals. Diffuse reflection spectra were obtained using a UV−vis spectrometer (Jasco, V-670 Spectrophotometer) and were converted from reflection to absorbance by the Kubelka−Munk method.[30,31]

SPS (GT Advanced Technologies, HP-20) was used to densify the stannite nanocrystals into dense polycrystalline specimens with nanoscale grains. SPS processing generates internal localized heating, thus allowing for the rapid, low temperature densification of fine-grain powders.[18,27] Since only the surface temperature of the nanopowders rises rapidly by self-heating, grain growth and impurity formation can be minimized by controlling the current. SPS densification was carried out at 60 MPa and 310 °C for 10 min with a current pulse ratio of 40:5 ms, resulting in phase-pure nanostructured polycrystalline specimens with a density of over 95% of the theoretical density, as determined by measuring the dimensions and mass of the pellets after SPS. The average grain size after densification was approximately 45 nm for $Cu_2ZnSnSe_4$ and 65 nm for $Ag_2ZnSnSe_4$, as calculated by applying the Scherrer equation to multiple reflections from the XRD data obtained after densification.[32] After washing, the products were clearly in powder form. In addition, no indication of graphitization was observed on the punch and die after SPS; therefore, we believe any remaining surfactants in our specimens after washing was very small and did not affect our transport data.

Temperature dependent four-probe resistivity, ρ, Seebeck coefficient, S (gradient sweep method), and steady-state κ measurements between 12 and 300 K were performed on both specimens while cooling. The measurements were conducted in a custom designed radiation-shielded vacuum probe with uncertainties of 4%, 6%, and 8% for ρ, S, and κ measurements, respectively,[33] on $2 \times 2 \times 5$ mm^3 parallelepipeds cut by a wire saw. Room temperature four-probe Hall measurements were conducted at multiple positive and negative magnetic fields in order to eliminate voltage probe misalignment.

■ RESULTS AND DISCUSSION

It is instructive to think of the three-dimensional stannite crystal lattice as being made of two-dimensional $[Ag_2Se_2]$ and $[ZnSnSe_2]$ layers, for $Ag_2ZnSnSe_4$, for example, alternating along the crystallographic c-axis. The unit cell representation of $Ag_2ZnSnSe_4$, shown in Figure 1, is composed of two different metal-chalcogenide, $[Ag_2Se_2]$ (A) and $[ZnSnSe_2]$ (B), layers with a stacking order of ···ABAB′AB··· along the crystallographic c axis. Layers B and B′ are the same morphologically, but B′ is translated relative to B by $\bar{4}$ symmetry along the crystallographic a axis in between $[Ag_2Se_2]$ layers. All atoms are surrounded by four other atoms in a tetrahedral coordination environment such that all transition metal atoms are surrounded by four Se atoms and the Se atoms are bounded by four metal atoms (two Ag, one Zn, and one Sn). By replacing Ag with Cu, the size of the unit cell increases, from 5.69 and 11.34 Å (for a and c, respectively, lattice constants that are in agreement with that reported previously[34]) to 5.79 and 11.45 Å, due to the larger size of the Ag atom compared with that of the Cu atom. The bond length of Ag−Se in $Ag_2ZnSnSe_4$ is longer than that of Cu−Se in $Cu_2ZnSnSe_4$[35] and results in a lowering of the energy level of the valence band maximum (VBM) which results in a larger band gap, as will be discussed below.

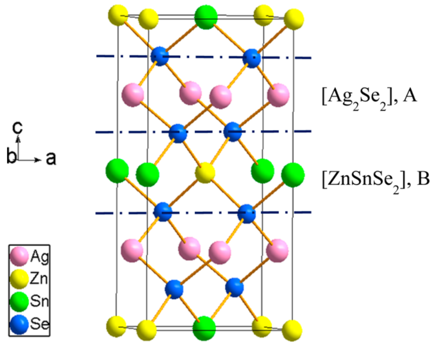

Figure 1. Crystal structure of $Ag_2ZnSnSe_4$. The dotted-dashed lines depict the two different metal-chalcogenide layers composed of $[Ag_2Se_2]$ and $[ZnSnSe_2]$.

Oleylamine is significant in the synthesis of these quaternary stannites as it acts as a surfactant, solvent, and reducing agent.[36,37] In the first stage of synthesis, metal acetates and metal chlorides dissolute with Oleylamine at an intermediate temperature, 110 °C, to form metal-oleylamine complexes that serve as secondary complex precursors. Later, while the solution is heated to a reaction temperature of 280 °C, the nanocrystals begin to form. Figure 2 shows the indexed XRD pattern of $Cu_2ZnSnSe_4$ and $Ag_2ZnSnSe_4$ nanocrystals. The successive spectra are normalized in intensity for clarity. The XRD data for $Ag_2ZnSnSe_4$ indicate the $I\bar{4}2m$ (#121) stannite phase. The XRD data for $Cu_2ZnSnSe_4$ also match the stannite phase; however, standard XRD cannot distinguish between the stannite and kesterite phases. Therefore, the presence of nanocrystals with the kesterite structure cannot be ruled out for the $Cu_2ZnSnSe_4$ nanocrystals.

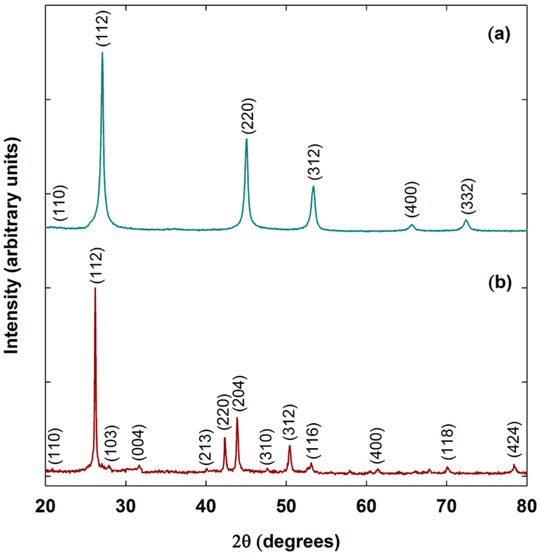

Figure 2. Indexed XRD patterns of (a) $Cu_2ZnSnSe_4$ and (b) $Ag_2ZnSnSe_4$ nanocrystals after synthesis.

Figure 3 shows high resolution TEM (HRTEM) and electron diffraction images of the quaternary stannite nanocrystals. TEM analyses indicate that the nanoparticles are spherical with an average size of 20 nm for $Cu_2ZnSnSe_4$ and 40 nm for $Ag_2ZnSnSe_4$. This result is consistent with that calculated from XRD employing the Scherrer equation. HRTEM analysis of the nanocrystals verified their tetragonal structure with lateral facets corresponding to (112) planes (0.327 and 0.341 nm d-spacing for $Cu_2ZnSnSe_4$ and

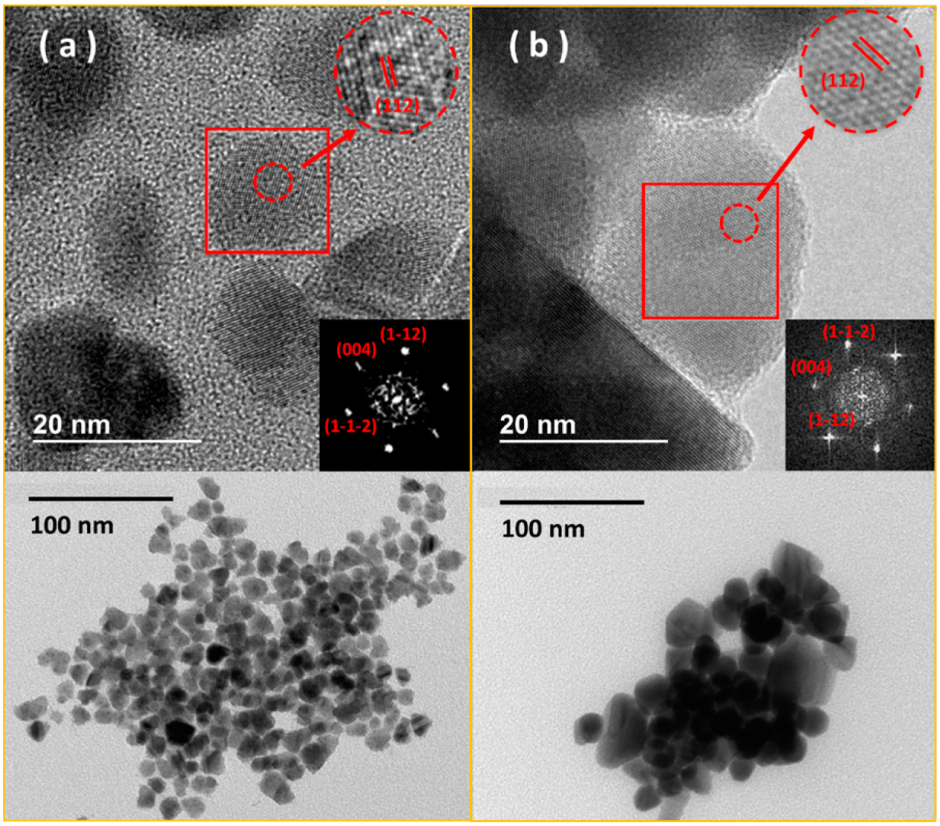

Figure 3. HRTEM and electron diffraction images of (a) $Cu_2ZnSnSe_4$ and (b) $Ag_2ZnSnSe_4$ nanocrystals.

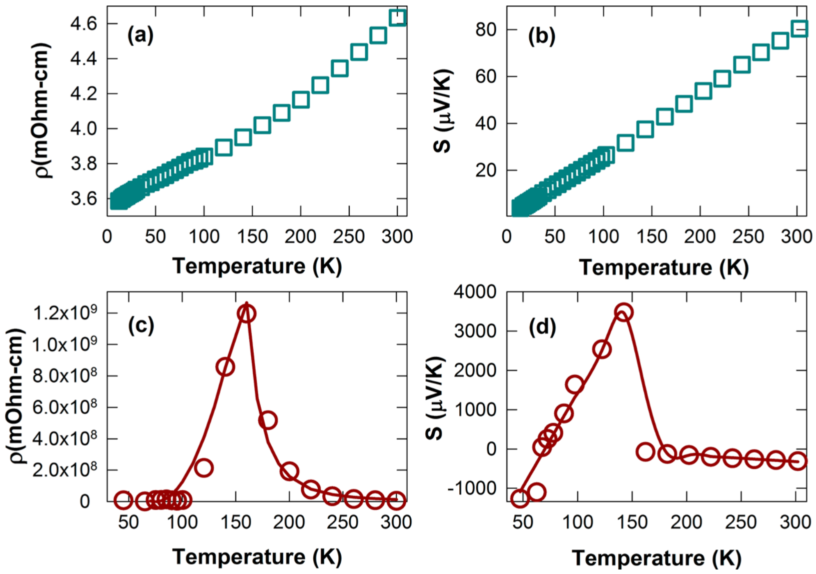

Figure 4. Temperature dependent ρ and S of $Cu_2ZnSnSe_4$, (a) and (b), and $Ag_2ZnSnSe_4$, (c) and (d), respectively. Solid lines are fits using the two-component model as described in the text.

$Ag_2ZnSnSe_4$, respectively). The power spectrum analysis of the lattice planes are denoted in the figures.

Figure 4 shows the low temperature ρ and S of the nanostructured polycrystalline bulk $Cu_2ZnSnSe_4$ and $Ag_2ZnSnSe_4$. Room temperature Hall data indicates p-type conduction for $Cu_2ZnSnSe_4$ and n-type conduction for $Ag_2ZnSnSe_4$. For $Cu_2ZnSnSe_4$ (Figure 4a,b), ρ and S increase with increasing temperature, with room temperature ρ and S values in strong agreement with that of previous results on nanostructured $Cu_2ZnSnSe_4$[38] while the room temperature values for bulk are 1000 mΩ·cm and 352 μV/K,[11] respectively. This degenerate semiconductor behavior has also been observed at higher temperatures.[38] As shown in Figure 4c, ρ of $Ag_2ZnSnSe_4$ exhibits a large anomalous peak at 160 K. The S values for $Ag_2ZnSnSe_4$ (Figure 4d) also show an anomalous temperature dependent behavior in the region of the "resistive" peak. This type of behavior has been previously described by a two-component model whereby polaronic-type charge carriers are presumed to be composite polarons consisting of electrons surrounded by phonons[39] and/or magnons.[40] Eu chalcogenides,[40,41] colossal magnetoresistance compounds,[42] and Ag-doped ZnO,[43] whose carriers are primarily magnetic polarons, pentatellurides (e.g., $ZrTe_5$ and $HfTe_5$),[44] whose carriers are lattice or dielectric polarons, and $SrTiO_3$ films,[45] whose polarons are affected by electrons and vacancies, all display similar temperature dependent transport. In the case of $Ag_2ZnSnSe_4$, the electron−phonon interaction may cause self-trapping of electrons that forms a conducting band at low temperatures.[40] At very low temperatures, the coherent excitation band formed by polarons grows narrower as the temperature increases thereby increasing ρ until reaching a maximum value. At higher temperatures, the polarons become less coherent due to absorption and inelastic emission of phonons resulting in a decrease in ρ with increasing temperature.[39,44] The zero crossing of S correlates very well with the peak in the ρ, and when the temperature is further decreased, S drops dramatically. The decreasing $\mathrm{d}S/\mathrm{d}T$ values below 100 K implies the existence of a negative peak at lower temperatures, as is the case for polaronic materials.[39]

The solid lines in Figure 4 are theoretical fits to the data using the two-component model where ρ and S can be expressed as[39,40]

$$\rho(T) = [f(T)/\rho_{\mathrm{lt}}(T) + \{1 - f(T)\}/\rho_{\mathrm{ht}}(T)]^{-1} \tag{1}$$

$$S(T) = [f(T)] \times [-cT] + [1 - f(T)] \times [S(\infty)] \tag{2}$$

where ρ_{lt} is the low-temperature itinerant-carrier ρ, ρ_{ht} is the high-temperature localized-carrier ρ, $f(T)$ is the fraction of the carriers that are in a metallic state, and c and $S(\infty)$ are constants determined by the S data. ρ_{lt}, ρ_{ht}, and $f(T)$ can be further expressed as

$$\rho_{\mathrm{ht}}(T) = A_\rho \times T \times \exp(E_\rho/kT) \tag{3}$$

$$\rho_{\mathrm{lt}}(T) = B_\rho \times T^2 \tag{4}$$

$$f(T) = \{\exp[(T - T_0)/\Delta] + 1\}^{-1} \tag{5}$$

where T_0 is the temperature where the "resistive" peak appears and A_ρ, E_ρ, B_ρ, and Δ are fitting parameters. From our fit to the data, Figure 4c,d, $A_\rho = 130.5$, $E_\rho/k = 1745$ K, $B_\rho = 2 \times 10^5$, $T_0 = 160$ K, $\Delta = 3.3$ K, $c = 0.48$, and $S(\infty) = -420$. The relatively large A_ρ and B_ρ values suggest a strong polaron effect. The value obtained for E_ρ, the polaron activation energy, is similar to that reported for $LaMnO_3$ ($E_\rho/k = 1276$ K)[46] which has been shown to have a strong adiabatic hopping of polarons and is consistent with large A_ρ and B_ρ values. The small transition width,[39,40] Δ, value is inferred by the sharp "resistive" peak while the ratio of the number of carriers to the number of sites, c,[40] indicates the polaron "band" to be about half full. $S(\infty)$ indicates the S value at temperatures high enough to release all the polarons from their trapped sites, room temperature from Figure 4.

Figure 5 shows the lattice thermal conductivity, κ_{L}, for both specimens. Employing the Wiedemann−Franz relation, the electronic contribution to κ, κ_{E}, can be estimated from Figure 4a,c by the equation $\kappa_{\mathrm{E}} = L_0\sigma T$ with the Lorenz number, L_0, taken to be 2.45×10^{-8} $\mathrm{V^2\ K^{-2}}$. Due to the relatively high ρ values, κ_{L} is the dominant contribution to κ in both specimens. The solid lines in Figure 5 are theoretical fits to the data using the Debye approximation[47]

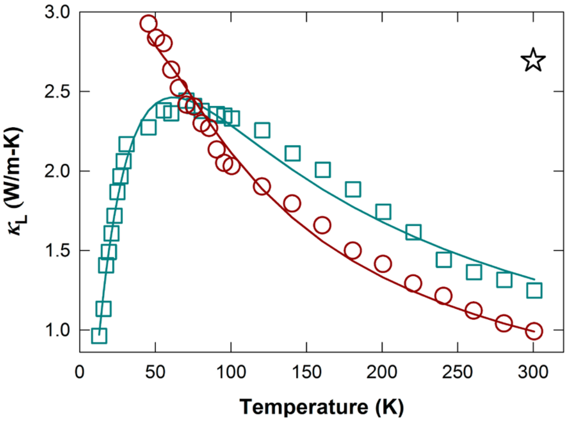

Figure 5. Temperature dependent κ of $Cu_2ZnSnSe_4$ (square) and $Ag_2ZnSnSe_4$ (circle). The solid lines are theoretical fits to the data using the Debye approximation. The star represents data for bulk $Cu_2ZnSnSe_4$.[11]

$$\kappa_{\mathrm{L}} = \frac{k_{\mathrm{B}}}{2\pi^2 \upsilon}\left(\frac{k_{\mathrm{B}}T}{\upsilon}\right)^3 \int_0^{\theta_{\mathrm{D}}/T} \frac{x^4 e^x}{\tau_{\mathrm{C}}^{-1}(e^x - 1)^2}\mathrm{d}x \tag{6}$$

where $x = \hbar\omega k B^{-1} T^{-1}$ is dimensionless, ω is the phonon frequency, θ_{D} is the Debye temperature, υ is the speed of sound, and τ_{C} is the phonon scattering relaxation time. In our fits, we use $\theta_{\mathrm{D}} = 302$ K and $\upsilon = 2861$ m/s, values reported for $Cu_2ZnSnSe_4$[48] since no such data is available for $Ag_2ZnSnSe_4$. τ_{C}^{-1} can be written as

$$\tau_{\mathrm{C}}^{-1} = \frac{\upsilon}{L} + A\omega^4 + B\omega^2 T \exp\left(-\frac{\theta_{\mathrm{D}}}{3T}\right) \tag{7}$$

where L is the grain size and the coefficients A and B are fitting parameters. Assuming three dominant phonon scattering mechanisms in the measured temperature range, the terms in eq 7 represent grain boundary scattering, point defect scattering, and Umklapp scattering, respectively. The fitting parameters, listed in Table 1, were uniquely defined using a minimization of the best sequence fit function compared to the data. The parameters shown in Table 1 yielded fit results with very strong agreement with the experimental data.

Table 1. Values of the κ_{L} Fit Parameters for $Cu_2ZnSnSe_4$ and $Ag_2ZnSnSe_4$

specimens	L (nm)	A (10^{-43} $\mathrm{s^3}$)	B (10^{-18} $\mathrm{s\ K^{-1}}$)
$Cu_2ZnSnSe_4$	45	179	13
$Ag_2ZnSnSe_4$	76	215	21

The average grain sizes, L, are in general agreement with that calculated from the XRD data obtained after SPS densification. The larger average grain size of the $Ag_2ZnSnSe_4$ specimen, as compared with that of the $Cu_2ZnSnSe_4$ specimen, results in higher κ_{L} values below 70 K for $Ag_2ZnSnSe_4$. Parameter A, point defect scattering, for the $Ag_2ZnSnSe_4$ specimen is larger than that of $Cu_2ZnSnSe_4$. This is likely due to the fact that Ag is much heavier and larger than Cu and may be the reason for the lower κ_{L} values for $Ag_2ZnSnSe_4$ than that for $Cu_2ZnSnSe_4$ above 70 K. The probability of anharmonic phonon scattering may however increase for $Ag_2ZnSnSe_4$ compared with that of $Cu_2ZnSnSe_4$ as implied by the larger fitting parameter B. The calculated Grüneisen parameter for $Cu_2ZnSnSe_4$ has been reported to be 2.37 at 300 K[49] while for $Cu_2ZnGeSe_4$ the

Grüneisen parameter has been experimentally reported to be 0.8.[29] In any case, no information is available on the Grüneisen parameter for $Ag_2ZnSnSe_4$, to the best of our knowledge. The star in Figure 5 denotes room temperature κ_L of bulk $Cu_2ZnSnSe_4$.[11] The κ_L values for nanostructured $Cu_2ZnSnSe_4$ are much lower than that of the bulk, as expected due to the additional grain boundary phonon scattering.[15,18,38] As a result, the room temperature figure of merit ($ZT = S^2T/\rho\kappa$, where T is the absolute temperature) of nanostructured $Cu_2ZnSnSe_4$, 0.02, is higher than that of the bulk, 0.001. For $Ag_2ZnSnSe_4$, $ZT = 2 \times 10^{-7}$ due to its very high ρ values.

Room temperature UV−vis spectra (Figure 6) indicated a band gap of 1.4 eV for $Ag_2ZnSnSe_4$ and 1.2 eV for $Cu_2ZnSnSe_4$.[50] This opening of the band gap in stannites with Ag instead of Cu may be due to a lowering of the energy level of the VBM, as has been observed in kesterite compounds, due to the longer bond lengths of Ag−Se (2.632 Å) as compared with that of Cu−Se (2.393 Å).[35] In addition, it was reported that $Ag_2ZnSnSe_4$ ($\Delta H_r = -28.6$ kJ/mol) is easier to decompose than $Cu_2ZnSnSe_4$ ($\Delta H_r = -84.1$ kJ/mol).[35] Our DTA results indicated a decomposition temperature of 470 °C for the $Cu_2ZnSnSe_4$ nanocrystals and 365 °C for the $Ag_2ZnSnSe_4$ nanocrystals, in agreement with that report.

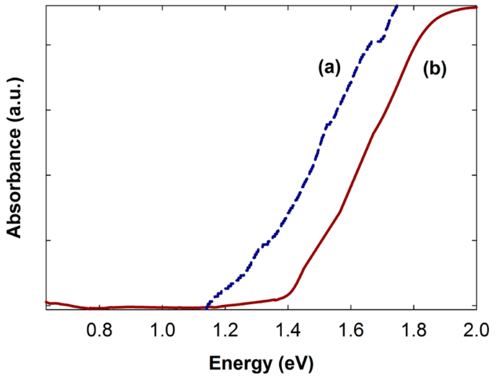

Figure 6. Room temperature UV−vis spectra of (a) $Cu_2ZnSnSe_4$ and (b) $Ag_2ZnSnSe_4$.

CONCLUSIONS

We report on the synthesis of $Cu_2ZnSnSe_4$ and $Ag_2ZnSnSe_4$ nanocrystals by a colloidal synthesis route. We also investigated the low temperature transport properties of dense polycrystalline nanostructured $Cu_2ZnSnSe_4$ and $Ag_2ZnSnSe_4$. $Cu_2ZnSnSe_4$ shows metallic-like conduction while $Ag_2ZnSnSe_4$ shows polaronic-type conduction. At room temperature, κ_L of $Cu_2ZnSnSe_4$ is greatly reduced as compared to that of the bulk due to enhanced grain boundary phonon scattering. Replacing Cu with Ag also resulted in additional point defect scatterings that contribute to lower κ_L for $Ag_2ZnSnSe_4$ compared to $Cu_2ZnSnSe_4$ above 70 K.

AUTHOR INFORMATION

Corresponding Author

*E-mail: gnolas@usf.edu.

Notes

The authors declare no competing financial interest.

ACKNOWLEDGMENTS

We acknowledge support by the II-VI Foundation Block-Gift Program for the crystal growth, powder XRD and characterization, transport measurements, and data analysis. The authors also acknowledge the U.S. Department of Energy, Basic Energy Sciences, Division of Materials Science and Engineering, under Award no. DE-FG02-04ER46145 for SPS processing.

REFERENCES

(1) Tanaka, K.; Oonuki, M.; Moritake, N.; Uchiki, H. Cu_2ZnSnS_4 Thin Film Solar Cells Prepared by Non-Vacuum Processing. *Sol. Energy Mater. Sol. Cells* **2009**, *93*, 583−587.

(2) Guo, Q.; Ford, G. M.; Yang, W. C.; Walker, B. C.; Stach, E. A.; Hillhouse, H. W.; Agrawal, R. Fabrication of 7.2% Efficient CZTSSe Solar Cells Using CZTS Nanocrystals. *J. Am. Chem. Soc.* **2010**, *132*, 17384−17386.

(3) Tsuji, I.; Shimodaira, Y.; Kato, H.; Kobayashi, H.; Kudo, A. Novel Stannite-Type Complex Sulfide Photocatalysts A^I-Zn-A^{IV}-S_4 (A^I = Cu and Ag; A^{IV} = Sn and Ge) for Hydrogen Evolution under Visible-Light Irradiation. *Chem. Mater.* **2010**, *22*, 1402−1409.

(4) Samanta, L. K.; Bhar, G. C. Optical Nonlinearity of Some Stannite and Famatinite Crystals. *Phys. Status Solidi A* **1977**, *41*, 331−337.

(5) Chen, S.; Gong, X. G.; Duan, C.-G.; Zhu, Z.-Q.; Chu, J.-H.; Walsh, A.; Yao, Y.-G.; Ma, J.; Wei, S.-H. Band Structure Engineering of Multinary Chalcogenide Topological Insulators. *Phys. Rev. B* **2011**, *83*, 245202/1−245202/5.

(6) Fries, T.; Shapira, Y.; Palacio, F.; Moron, M. C.; McIntyre, G. J.; Kershaw, R.; Wold, A.; McNiff, E. J. Magnetic Ordering of the Antiferromagnet Cu_2MnSnS_4 from Magnetization and Neutron-Scattering Measurements. *Phys. Rev. B* **1997**, *56*, 5424−5431.

(7) Nenert, G.; Palstra, T. T. M. Magnetoelectric and Multiferroic Properties of Ternary Copper Chalcogenides $Cu_2M^{II}M^{IV}S_4$. *J. Phys.: Cond. Matter* **2009**, *21*, 176002/1−176002/6.

(8) Liu, M.-L.; Huang, F.-Q.; Chen, L.-D.; Chen, I-W. A Wide-Band-Gap p-Type Thermoelectric Material Based on Quaternary Chalcogenides of Cu_2ZnSnQ_4 (Q=S,Se). *Appl. Phys. Lett.* **2009**, *94*, 202103−202105.

(9) Ibanez, M.; Cadavid, D.; Zamani, R.; Garcia-Costello, N.; Izkuierdo-Roca, V.; Li, W.; Fairbrother, A.; Prades, J. D.; Shavel, A.; Arbiol, J.; Perez-Rodriguez, A.; Morante, J. R.; Cabot, A. Composition Control and Thermoelectric Properties of Quaternary Chalcogenide Nanocrystals: The Case of Stannite $Cu_2CdSnSe_4$. *Chem. Mater.* **2012**, *24*, 562−570.

(10) Dong, Y.; Khabibullin, A. R.; Wei, K.; Ge, Z.; Martin, J.; Salvador, J. R.; Woods, L. M.; Nolas, G. S. Synthesis, Transport Properties, and Electronic Structure of $Cu_2CdSnTe_4$. *Appl. Phys. Lett.* **2014**, *104*, 252107/1−252107/4.

(11) Dong, Y.; Wang, H.; Nolas, G. S. Synthesis and Thermoelectric Properties of Cu Excess $Cu_2ZnSnSe_4$. *Phys. Status Solidi RRL* **2014**, *8*, 61−64.

(12) Heremans, J. P.; Thrush, C. M.; Morelli, D. T. Thermopower Enhancement in Lead Telluride Nanostructures. *Phys. Rev. B* **2004**, *70*, 115334/1−115334/5.

(13) Martin, J.; Wang, L.; Chen, L. D.; Nolas, G. S. Enhanced Seebeck Coefficient through Energy-Barrier Scattering in PbTe Nanocomposites. *Phys. Rev. B* **2009**, *79*, 115311/1−115311/5.

(14) Biswas, K.; He, J.; Blum, I. D.; Wu, C.; Hogan, T. P.; Seidman, D. N.; Dravid, V. P.; Kanatzidis, M. G. High-Performance Bulk Thermoelectrics with All-Scale Hierarchical Architectures. *Nature* **2012**, *489*, 414−418.

(15) Nolas, G. S.; Sharp, J. W.; Goldsmid, H. J. *Thermoelectrics: Basics Principles and New Materials Developments*; Springer Publications: Berlin, 2001.

(16) Snyder, G. J.; Toberer, E. S. Complex Thermoelectric Materials. *Nat. Mater.* **2008**, *7*, 105−114.

(17) Sootsman, J. R.; Chung, D. Y.; Kanatzidis, M. G. New and Old Concepts in Thermoelectric Materials. *Angew. Chem., Int. Ed. Engl.* **2009**, *48*, 8616−8639.

(18) Datta, A.; Popescu, A.; Woods, L.; Nolas, G. S. In *CRC Handbook on Thermoelectrics and Its Energy Harvesting on Materials, Preparation and Characterization*; Rowe, D. M., Ed.; Taylor & Francis: London, 2012; Chapter 14.

(19) Heremans, J. P.; Dresselhaus, M. S.; Bell, L. E.; Morelli, D. T. When Thermoelectrics Reached the Nanoscale. *Nat. Nanotechnol.* **2013**, *8*, 471−473.

(20) Popescu, A.; Woods, L. M.; Martin, J.; Nolas, G. S. Model of Transport Properties of Thermoelectric Nanocomposite Materials. *Phys. Rev. B* **2009**, *79*, 205302/1−205302/7.

(21) Dresselhaus, M. S.; Chen, G.; Tang, M. Y.; Yang, R.; Lee, H.; Wang, D.; Ren, Z. F.; Fleurial, J.-P.; Gogna, P. New Directions for Low-Dimensional Thermoelectric Materials. *Adv. Mater.* **2007**, *19*, 1043−1053.

(22) Kanatzidis, M. G. Nanostructured Thermoelectrics: The New Paradigm? *Chem. Mater.* **2010**, *22*, 648−659.

(23) Vineis, C. J.; Shakouri, A.; Majumdar, A.; Kanatzidis, M. G. Nanostrctured Thermoelectrics: Big Efficiency Gains from Small Features. *Adv. Mater.* **2010**, *22*, 3970−3980.

(24) Chen, G.; Dresselhaus, M. S.; Fleurial, J.-P.; Caillat, T. Recent Developments in Thermoelectric Materials. *Int. Mater. Rev.* **2003**, *48*, 45−66.

(25) Biswas, K.; He, J.; Blum, I. D.; Wu, C.; Hogan, T. P.; Seidman, D. N. High-Performance Bulk Thermoelectrics with All-Scale Hierarchical Architectures. *Nature* **2012**, *489*, 414−418.

(26) Minnich, A. J.; Dresselhaus, M. S.; Ren, Z. F.; Chen, G. Bulk Nanostructured Thermoelectric Materials: Current Research and Future Prospects. *Energy Environ. Sci.* **2009**, *2*, 466−479.

(27) Wei, K.; Martin, J.; Nolas, G. S. Synthesis, SPS Processing and Low Temperature Transport Properties of Polycrystalline $FeSb_2$ with Nano-Scale Grains. *Mater. Lett.* **2014**, *122*, 289−291.

(28) Shavel, A.; Cadavid, D.; Ibáñez, M.; Carrete, A.; Cabot, A. Continuous Production of Cu_2ZnSnS_4 Nanocrystals in a Flow Reactor. *J. Am. Chem. Soc.* **2012**, *134*, 1438−1441.

(29) Zeier, W. G.; LaLonde, A.; Gibbs, Z. M.; Heinrich, C. P.; Panthöfer, M.; Snyder, G. J.; Tremel, W. Influence of a Nano Phase Segregation on the Thermoelectric Properties of the p-Type Doped Stannite Compound $Cu_{2+x}Zn_{1-x}GeSe_4$. *J. Am. Chem. Soc.* **2012**, *134*, 7147−7154.

(30) Kubelka, P.; Munk, F. The Kubelka-Munk Theory of Reflectance. *Ein Beitrag zur Optik der Farbanstriche, Zeits. f. Techn. Physik* **1931**, *12*, 593−601.

(31) López, R.; Gómez, R. Band-Gap Energy Estimation from Diffuse Reflectance Measurements on Sol−Gel and Commercial TiO_2: A Comparative Study. *J. Sol-Gel Sci. Technol.* **2012**, *61*, 1−7.

(32) Patterson, A. The Scherrer Formula for X-ray Particle Size Determination. *Phys. Rev.* **1939**, *56*, 978−982.

(33) Martin, J.; Nolas, G. S.; Wang, H.; Yang, J. Thermoelectric Properties of Silicon-Germanium Type I Clathrates. *J. Appl. Phys.* **2007**, *102*, 103719/1−103719/6.

(34) Olekseyuk, I. D.; Gulay, L. D.; Dydchak, I. V.; Piskach, L. V.; Parasyuk, O. V.; Marchuk, O. V. Single Cystal Preparation and Crystal Structure of the $Cu_2Zn/Cd,Hg/SnSe_4$ Compounds. *J. Alloys and Comp.* **2002**, *340*, 141−145.

(35) Nakamura, S.; Maeda, T.; Tabata, T.; Wada, T. First-Principles Study of Indium-Free Photovoltaic Compounds $Ag_2ZnSnSe_4$ and $Cu_2ZnSnSe_4$. *IEEE Photovoltaic Spec. Conf., 37th* **2011**, *11*, 002771−002774.

(36) Joo, J.; Na, H. B.; Yu, T.; Yu, J. H.; Kim, Y. W.; Wu, F.; Zhang, J. Z.; Hyeon, T. Generalized and Facile Synthesis of Semiconducting Metal Sulfide Nanocrystals. *J. Am. Chem. Soc.* **2003**, *125*, 11100−11105.

(37) Mourdikoudis, S.; Liz-Marzan, L. M. Oleylamine in Nanoparticle Synthesis. *Chem. Mater.* **2013**, *25*, 1465−1476.

(38) Fan, F.-J.; Wang, Y.-X.; Liu, X.-J.; Wu, L.; Yu, S.-H. Large-Scale Colloidal Synthesis of Non-Stoichiometric $Cu_2ZnSnSe_4$ Nanocrystals for Thermoelectric Applications. *Adv. Mater.* **2012**, *24*, 6158−6163.

(39) Rubinstein, M. $HfTe_5$ and $ZrTe_5$: Possible Polaronic Conductors. *Phys. Rev. B* **1999**, *60*, 1627−1632.

(40) Rubinstein, M. Two-Component Model of Polaronic Transport. *J. Appl. Phys.* **2000**, *87*, 5019−5021.

(41) Laks, B.; Goncalves da Silva, C. E. T. Metal-Insulator Transition in Eu-Rich EuO. *Phys. Rev. Lett.* **1976**, *36*, 1204−1206.

(42) Srivastava, C. M.; Srivastava, N. B.; Singh, L. N.; Bahadur, D. Small Polaron Transport and Colossal Magnetoresistance in $La_{2/3}Ca_{1/3}MnO_3$. *J. Appl. Phys.* **2009**, *105*, 093908/1−093908/7.

(43) He, M.; Tian, Y. F.; Springer, D.; Putra, I. A.; Xing, G. Z.; Chia, E. E. M.; Cheong, S. A.; Wu, T. Polaronic Transport and Magnetism in Ag-Doped ZnO. *Appl. Phys. Lett.* **2011**, *99*, 222511/1−222511/3.

(44) Littleton, R. T., IV; Tritt, T. M.; Kolis, J. W.; Ketchum, D. R.; Lowhorn, N. D.; Korzenski, M. B. Suppression of the Resistivity Anomaly and Corresponding Thermopower Behavior in the Pentatelluride System by the Addition of Sb: $Hf_{1-X}Zr_XTe_{5-Y}Sb_Y$. *Phys. Rev. B* **2001**, *64*, 121104/1−121104/4.

(45) Choi, W. S.; Yoo, H. K.; Ohta, H. Polaron Transport and Thermoelectric Behavior in La-Doped $SrTiO_3$ Thin Films with Elemental Vacancies. *Adv. Funct. Mater.* **2015**, *25*, 799−804.

(46) Jaime, M.; Lin, P.; Chun, S. H.; Salamon, M. B.; Dorsey, P.; Rubinstein, M. Coexistence of Localized and Itinerant Carriers Near T_C in Calcium-Doped Manganites. *Phys. Rev. B* **1999**, *60*, 1028−1032.

(47) Callaway, J. Model for Lattice Thermal Conductivity at Low Temperatures. *Phys. Rev.* **1959**, *113*, 1046−1051.

(48) Bensalem, S.; Chegaar, M.; Maouche, D.; Bouhemadou, A. Theoretical Study of Structural, Elastic and Thermodynamic Properties of CZTX (X = S and Se) Alloys. *J. Alloys and Comp.* **2014**, *589*, 137−142.

(49) He, X.; Pi, J.; Dai, Y.; Li, X. Elastic and Thermo-Physical Properties of Stannite-Type Cu_2ZnSnS_4 and $Cu_2ZnSnSe_4$ from First-Principles Calculations. *Acta Metall. Sin. (Engl. Lett.)* **2013**, *26*, 285−292.

(50) Wei, K.; Nolas, G. S. Synthesis, Characterization and Alloying of Cu_2ZnSnQ_4 (Q=S, Se and Te) Nanocrystals. *J. Solid State Chem.* **2015**, *226*, 215−218.

DOI: 10.1021/acsami.5b01617
ACS Appl. Mater. Interfaces 2015, 7, 9752−9757